JOURNAL OF AIRCRAFT
Vol. 47, No. 5, September–October 2010

Influence of Differential Spoiler Settings on the Wake Vortex Characterization and Alleviation

Omer A. Elsayed,* Waqar Asrar,† and Ashraf A. Omar‡
International Islamic University Malaysia, Gombak, Kuala Lumpur 53100
and
Kijung Kwon§
Korea Aerospace Research Institute, Deajeon 305-333, Republic of Korea

DOI: 10.2514/1.C000258

Experimental investigations using particle image velocimetry technique have been carried out for the evaluation of the differential spoiler setting capabilities in modifying the spanwise wing load and further reduce the wake vortex hazard. The aircraft half model (at high lift configuration) was investigated for two differential spoiler settings. Results reveal a noticeable inboard shift of spanwise wing loading. Implementation of a differential spoiler setting results in a substantial redistribution of the flap tip vortex circulation with an increase in the diameter of the merged vortex by a factor of up to 2.72 relative to the undisturbed flap tip vortex. Inspection of the cross-stream distribution of axial vorticity shows a reduction by a factor of up to 2.33 in the peak vorticity value. A 44% decrease of the maximum crossflow velocity relative to the undisturbed flap tip vortex crossflow velocity was recorded for the case of deployed spoilers. Finally assessment of the differential spoiler setting capabilities as a wake vortex attenuation device reveals that, while position of the maximum induced rolling moments in the flap tip area is little influenced by the differential spoiler setting, the maximum induced rolling moment coefficient was reduced to nearly one third of the undisturbed flap tip vortex value.

Nomenclature

AR	=	aspect ratio
b	=	wing span
bf, bg	=	span of the follower and generating wing
$b_f/2$	=	semispan of the follower wing
C_L	=	wing lift coefficient
C_{lf}	=	induced rolling moment coefficient
$C_{lf\,\max}$	=	maximum induced rolling moment coefficient
$C_{lf\alpha}$	=	lift gradient
$\bar{c}$	=	mean wing aerodynamic chord
d	=	vortex diameter
$L'(y)$	=	lift per unit span
Re_c	=	Reynolds number based on mean aerodynamic chord
r	=	radial distance
SG	=	specific gravity
V_c	=	crossflow velocity of the vortex
$V_{c\text{-Max}}$	=	maximum crossflow velocity of the vortex
$V_{c\text{-Min}}$	=	minimum crossflow velocity of the vortex
V_∞	=	air speed
v_θ	=	tangential velocity
$v_{\theta\max}$	=	maximal tangential velocity
v, w	=	velocity in the spanwise and vertical directions
x, y, z	=	axes of flight direction, spanwise direction and in the vertical direction
y', z'	=	coordinates in the spanwise and in vertical direction fixed at the following wing center
α	=	angle of attack
$\Gamma(y)$	=	circulation at local spanwise station
Γo	=	circulations of the inner vortex
ΔV_{dis}	=	uncertainties on the particle image velocimetry distances
ΔV_i	=	total uncertainty in the mean velocity measurements from particle image velocimetry
ΔV_θ	=	uncertainty in the tangential velocity
ΔX, ΔY	=	uncertainties on the distances in horizontal and vertical direction
$\Delta\xi$	=	uncertainty in vorticity
λ	=	wing taper ratio
ξ	=	axial vorticity
ξ_{Peak}	=	peak axial vorticity value
ρ	=	air density
$(\sigma Vi)_{\text{avg}}$	=	average standard deviation in the velocity

Received 13 January 2010; revision received 26 March 2010; accepted for publication 26 March 2010.

*Research Assistant, Kulliyyah of Engineering, P.O. Box 10, 50728.
†Professor, Kulliyyah of Engineering, P.O. Box 10, 50728.
‡Professor, Kulliyyah of Engineering, P.O. Box 10, 50728. Member AIAA.
§Senior Researcher, Aerodynamics Department, 45 Eoeun-dong, Yuseong-gu.

I. Introduction

WAKE vortices are initiated due to lift generation which as well implies a generation of circulation in the flow that they travel through. For large aircraft these vortices tend to be strong and persistent, thus, they can pose a serious threat to any smaller aircraft that may encounter them. This problem is referred to as the wake vortex hazard. Serious problems due to wake vortices were first recognized back in the 1970s when the Boeing 747 came into service. To avoid such wake vortex encounters, follower aircraft must preserve a safe distance from a landing aircraft up ahead of them. These standard separation distances limit the capacity of many airports already in the present use. Furthermore, introduction of 400+ passenger aircraft with continuously growing air traffic at a rate of 5% per year, separation rules of today are considered increasingly inadequate to cope with air traffic needs for future.

Control strategies of wake vortices ranges from passive control, using spanwise wing load modifications, up to active control, using control-surface oscillations [1]. Earlier studies have shown that by modifying the wingspan loading, the typical rotational velocities within the originated wake can be reduced significantly [2,3]. Changes in the wingspan loading of an aircraft can be obtained by means of differential flap setting (DFS). The DFS can also act on the roll up process and on the stability of the wake vortices by producing corotating or counter- rotating multiple vortices, thus facilitating the

onset of instability mechanisms [4,5]. Quite large values for the inboard counter rotating circulation strength are needed [6] that are not really manageable on an existing aircraft [7]. Consequently for practical applications, substitution of DFS by differential spoiler setting (DSS) looked encouraging.

Early work on effectiveness of wing spoilers was investigated by [8] as a possible method of vortex attenuation since the deflection of the spoiler will inject turbulence into the wake as well as alter the span load distribution. Langley V/STOL tunnel was used to determine by the trailing wing sensor technique, the trailing-vortex-alleviation effectiveness of various segments of the flight spoilers of Boeing 747 configuration. Results from tests of two of the flight-spoiler configurations made over a deflection range from 0 to 45° indicate that essentially all the reduction in induced rolling moment on the trailing model was realized at a spoiler deflection of about 30° at a downstream distance of about seven wing spans behind the transport aircraft model.

Flight testing using Boeing 747 aircraft was initiated at Dryden [9]. In the flight program, NASA T-37 and Learjet aircraft were used to penetrate the trailing vortex. Tests without the spoilers of the Boeing 747 deployed produced violent roll upset problems for the T-37 aircraft at a distance of approximately 3 miles. With two spoilers on the outer wing panels deflected, the T-37 could fly within a distance of 3 miles and not experience the upset problem. Although initial flight results verified the effectiveness of the spoiler concept, additional flight tests indicated that the effectiveness was sometimes not repeatable (probably because of atmospheric conditions) at low altitudes. Recently, work in the AWIATOR program [7] focused on wing span loading concept that uses existing control surfaces on the A340, such as DFS or DSS. Flight tests were conducted during the first AWIATOR flight test campaign in 2003 [7]. It was not possible to use DFS, but specific DSS configurations were designed and tested as an alternative to mimic inboard and outboard loaded flap settings. Unfortunately, because of weather effects (variations in turbulence levels and stratification) the Lidar data were not able to differentiate in vortex strength between the various cases. However, the downward displacement of the vortices seemed to indicate the expected tendency, with the inboard loaded case moving faster downward. In subsequent flight test in 2006 [7], inboard loading flaps configuration, tested in relatively calm air shows on the time average a 20% earlier vortex linking occurred compared with baseline configuration.

Tests at the University of Munich used a multiwire hotwire probe to measure unsteady flow phenomena in near and extended near wakes were conducted. It reveals that turbulence intensity distributions for spoiler number 6 (outboard spoiler deflected at 20°) configurations at two spans downstream distance, increases significantly with respect to the baseline configuration. Also an earlier merging of the outer and inner flap vortex with a fatter vortex core and a lower peak velocity were observed in the Hamburg ship model basin towing tank test, National Aerospace Laboratory (The Netherlands) (NLR) executive summary report [7].

Early studies focused on evaluation of flight-spoiler wake vortex attenuation capabilities through direct measurement of the rolling moment experienced by trailing wing sensor technique. While recent information on DSS available in public domain is limited. Therefore understanding the topology and structure details of the wake vortex with deployed spoilers (DSS) configurations is a matter yet to be explored. Furthermore justification of the quick replacement of the DFS with DSS is to be carried out bearing in mind that the two approaches are of a different wake vortex control background. Finally capability of DSS on span load modification along with its effectiveness as a wake vortex alleviation device is investigated.

II. Experimental Setup

A. Half Aircraft Model

Tests have been performed using a generic half aircraft model, a schematic drawing with the control surfaces and spoilers is shown in Fig. 1. The half model has a span of 1.115 and 0.3682 m mean aerodynamic wing chord. The half span was measured from the fuselage center line to the furthest spanwise point on the wing tip. The wing is equipped with a fully deployable single slat which extends along the entire wing span leading edge, a single aileron and a single flap to perform the investigation of a high lift configuration (HLC). Moreover the wing is equipped with six segments of a conventional flight spoiler. They are fitted on the upper surface of the wing with a

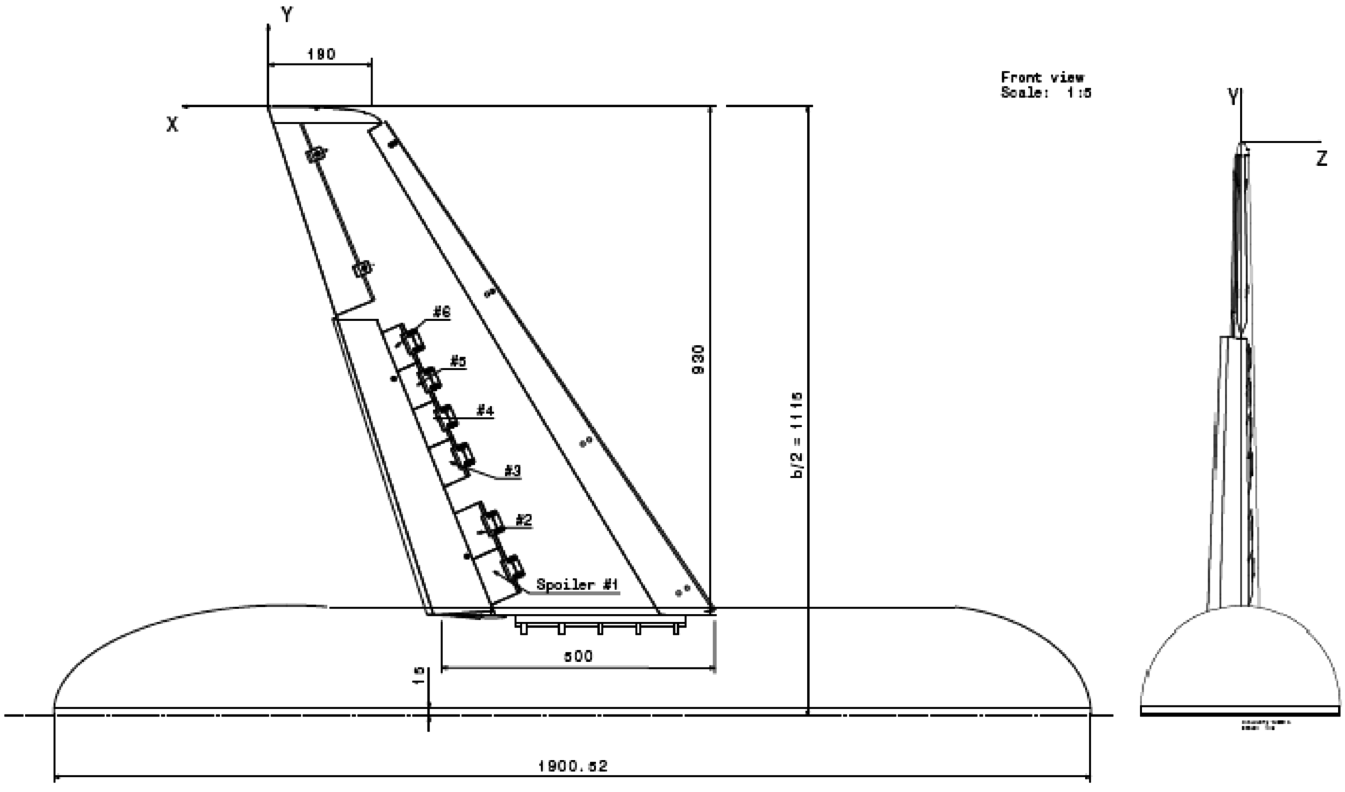

Fig. 1 Schematic drawing of the half model (all dimensions are in mm).

length of 11.8 and 11.1% for spoiler numbers 5 and 6, respectively. They were hinged at 62.5% measured from the leading edge of the wing. A rounded tip fairing was added to the wing tip and the wing has dihedral angle of 33.46° with a tapered NACA 23012 profile. Wing taper ratio equal to $\lambda = 0.38$ (root chord of 0.5 m and tip chord of 0.190 m), and has an aspect ratio of AR = 6.137.

B. Wind Tunnel

All experiments were performed in the International Islamic University Malaysia closed circuit low speed wind tunnel. With a test section of 1.5 by 2.3 m in cross section and a length of 6 m. Honeycomb and fine screens are mounted before the contraction inlet to reduce the turbulence and flow irregularities. This leads to a low freestream turbulence intensity of 0.07% in the flow-direction, 0.1% in the lateral-direction and 0.11% in the vertical direction. The half model is mounted on 15 mm peniche at the turn table positioned on the tunnel floor and extends vertically into the test section with the wing-tip point towards the ceiling of the wind tunnel. The test section is equipped with a six-component force-balance which enables to measure all aerodynamic loads on the model.

C. Measurement Conditions

The aircraft half model has been tested in a typical HLC named hereafter as baseline configuration. The HLC device settings were 1) slat at 15° and 2) flap at 20°. The DSS with spoiler numbers 5 and 6 deflected both at 30° named hereafter inboard loading case 1 and further they were deflected at 40° named hereafter inboard loading case 2. Fairing as well as small discrete supports allows adjusting the various setting. Picture of the inboard loading case 1 is shown in Fig. 2 as a model for both inboard loading cases.

The angle of attack was set to =7°, giving a target lift coefficient. C_L-α Curves obtained from external balance measurement are shown in Fig. 3. All model configurations were primarily tested on this target lift coefficient value (It was found that increasing the angle of attack by 2° will recover the target lift value for DSS tested configurations.) The experiments have been done for all configurations at a freestream velocity of $V_\infty = 12$ (m/s), corresponding to Reynolds number $Re_c = 2.82 \times 10^5$, based on the wing mean aerodynamic chord. The surface flow has been monitored by using tufts for regional laminar separation which has proven, that attached flow is present on wing upper surface and control surfaces areas. The origin of the coordinates is located at the wing-tip trailing edge. The x, y and z coordinates are aligned with the streamwise, spanwise and vertical directions, respectively. Clockwise wing rotation about the y-coordinate axis (along the spanwise direction) is considered for a positive angle of attack.

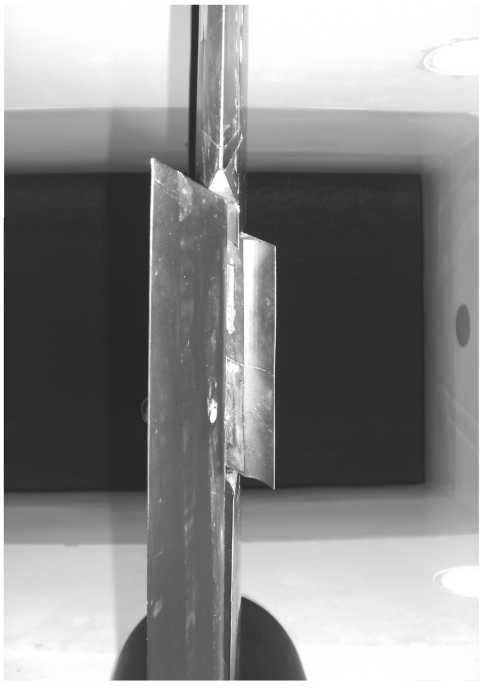

Fig. 2 Picture of inboard loading case 1.

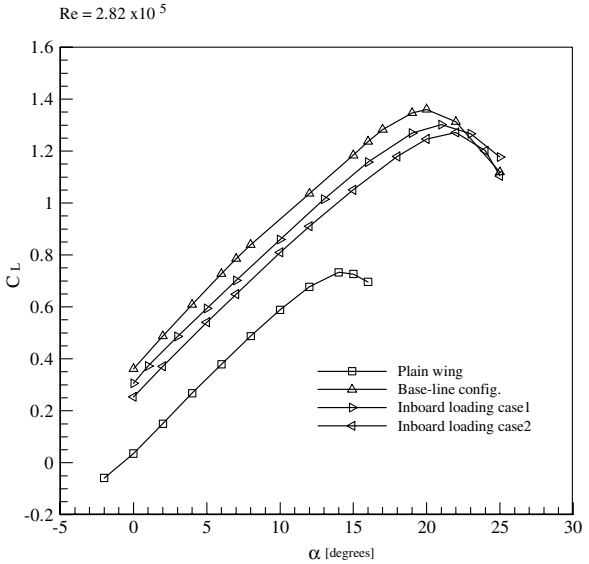

Fig. 3 Curves at $Re = 2.82 \times 10^5$ ($CL \sim \alpha$).

D. Particle Image Velocimetry Experiment

Particle image velocimetry (PIV) measurements were used to obtain the crossflow velocities of the wing tip and (flap tips) vortices. Dantec Dynamics PIV system, consisting of a high power pulsed laser was used to conduct the experiments. The wake vortex has been measured at four crossflow planes, $x/b = 0.317$, 0.438, 0.649 and 1.062, where b is the wing span. Illustration of the measurement cross-section planes are shown in Fig. 4. To illuminate the flow, a light sheet is obtained from the beam of a Solo PIV Nd:YAG laser system120 XT and directed perpendicular to the airflow.

The PIV images of the light sheet were recorded using a Flow Sense M2 8 bit charge-coupled device (CCD) camera (1600× 1168 pixels) with Micro-Nikkor 60 mm camera lens. Two CCD cameras were used at the same time to locate the wing/flap tip vortices position. Further measurements were carried out with one camera output. The wind tunnel was globally seeded with SAFEX FLUID fog particles. The fog droplets remained suspended as the flow circulated through the closed-loop wind tunnel. The seeding particles have a specific gravity SG = 1 and average diameter of 1 μm. They were injected into the flow downstream of the model so that they were fully mixed before reaching the model. Although the vortex has strong centrifugal force, particles are small enough to follow the flow structure. A picture of the PIV experiments (half model, CCD camera's and laser head) as they appear in the test section is shown in Fig. 5. Time delay between successive pulses was μs thus the particle would travel 21% of the light sheet thickness ($\sim$2 mm).

This will prevent out-of-plane particles and hence reduce the error due to the streamwise extent of the measurement volume. A field of view typically of (189.06 138.01) mm with 8.4627 (pixel/mm) spatial resolution, was obtained in the images which were recorded and further post processed to obtain the instantaneous two-dimensional velocity vectors with cross-correlation on a rectangular window size of 32×32 pixels and 50% increment. Image interrogation was repeated three-times in order to increase the data yield due to higher amount of matched particle images along with the reduction of bias error. Eight closest neighbors of a correlation were used for peak detection. There are a variety of sources of error in velocity measurements using PIV.

An estimation of the uncertainty is made here by considering the statistical uncertainty, the uncertainty in the wing angle of attack and

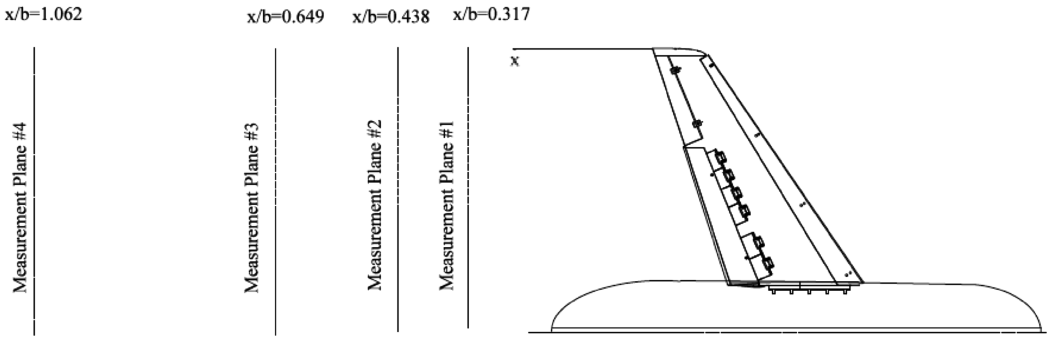

Fig. 4 Illustration of the measurement cross-section planes.

Fig. 5 PIV experiment setup.

uncertainties on the distances ΔX and ΔY. Statistical uncertainty in the mean velocity measurements from PIV, can be estimated using average standard deviation in velocity $(\sigma Vi)_{\text{avg}} = 0.634$ (m/s) for the HLC test cases. Hundred samples were taken, thus $(\Delta V_i) = \pm 0.1242$ (m/s) based on (95%) confidence level. The uncertainty in the wing angle of attack contributed to the uncertainty in the tangential velocity components by affecting the circulation in the vortex. The sensitivity in angle of attack of the root section lift coefficient (two-dimensional flow is considered at the root section) is estimated as $\partial C_l/\partial \alpha_{\text{NACA23012}} = 0.0825$.

This can be converted to circulation sensitivity through

$$\partial \Gamma_o/\partial \alpha = 1/2 V_\infty c \partial C_l/\partial \alpha \tag{1}$$

and further converted to tangential velocity sensitivity through

$$\partial V_\theta/\partial \alpha = 1/2\pi r \partial \Gamma_o/\partial \alpha \tag{2}$$

The value of r was taken to be to be 11 mm which was roughly equal to the vortex internal core radius based on maximum tangential velocity. Substituting these values into Eq. (2), the sensitivity is

$$|\partial V_\theta/\partial \alpha| = 2.6356 \text{ (m/s)/ deg} \tag{3}$$

The uncertainty in the angle of attack is $\pm 0.05°$, hence the uncertainty in the tangential velocity due to uncertainty in the angle of attack is $\Delta V_\theta = \pm 0.1318$ (m/s). The relative uncertainty in the velocity due to uncertainty in the displacements ΔX and ΔY can be expressed as $\delta \Delta X'/\Delta X = \sqrt{(0.5^2 \text{ pix}/3^2)} = 0.1667$ pix, 0.014445 mm can be considered as an uncertainty in the distances ΔX and ΔY which results in $\Delta V_{\text{dis}} = 0.5625$ (m/s). Adding to total uncertainty in velocity, $\Delta V_i = \pm\sqrt{0.13178^2 + 0.1242^2 + 0.5625^2} = \pm 0.5909$ (m/s). This implied an uncertainty in vorticity, $\Delta \xi = \pm 312.97$ s^{-1}.

III. Meandering of the Vortex Cores

Figure 6 compares the vortex center position of the time-averaged field to the vortex center of the instantaneous flow fields for 50 to 75 realizations. The time-averaged vortex center is shown with a circle symbol whereas the instantaneous vortex centers are shown with delta symbols. Results reveal a periodic movement of the vortex center and hence vortex center values are repeated frequently. The error bars present the standard deviation of the core movement in lateral and vertical directions. Using the standard deviation to calculate the amplitude of wandering, this quantity is estimated at 43% of the core radius for wing-tip vortex at HLC (see Fig. 6a).

Introduction of the spoilers increases the wing-tip vortex wandering amplitude. It reaches 47 and 59% of the wing-tip vortex core radius for inboard loading case 1 and 2, respectively, as can be seen in Fig. 6b and 6c. However, the wandering amplitude for the flap tip vortex core is much more significant. It reaches a value of 170% of the flap vortex core radius at HLC see Fig. 6d. The above results show that the time-averaged fields are heavily influenced by the vortex wandering. Nevertheless, the examination of the time-averaged fields can be supported by the analysis of the instantaneous fields. Velocity data were corrected for the effects of wandering by averaging together a number of individual realizations, spatially shifted to ensure that instantaneous vortex center were coincident and hence removing the effect of wandering upon the data.

IV. Modification of Spanwise Wing Load Distribution

The strength of the trailing edge vortex system downstream of the configuration is proportional to wing lift, while its topology will largely depend on the spanwise lift distributions of the wing [10]. To measure the spanwise load distributions on the half model wing, a wake integration technique based on the control volume approach was used where the momentum deficit parallel to the freestream is evaluated within the model wake. PIV was used to obtain the crossflow velocity in planes 0.438 span downstream of the half model in HLC as well as in an inboard loading case 1 and 2. The calculation of the lift distribution across the wing is obtained using wake integration of vorticity and is a result of Prandtl's classical lifting line theory for inviscid, incompressible flow [11], where the wing is represented by a distributed circulation along the wing. Once the value of bound circulation at the transverse point y, on the lifting line is known, the Kutta–Joukowski theorem [Eq. (4)] yields the lift per unit span at that y position along the lifting line:

$$L'(y) = \rho_\infty V_\infty \Gamma(y) \tag{4}$$

here ρ_∞, V_∞ and $\Gamma(y)$ are standing for freestream density, freestream velocity and local spanwise circulation value. The streamwise component of vorticity in the center of each cell in the uniform velocity grid, with the velocity components $v_{j,k}$ and $w_{j,k}$, is approximated by

$$\xi_{j+1/2,k+1/2} = \frac{\Gamma_{j+1/2,k+1/2}}{\Delta y \Delta z} \tag{5}$$

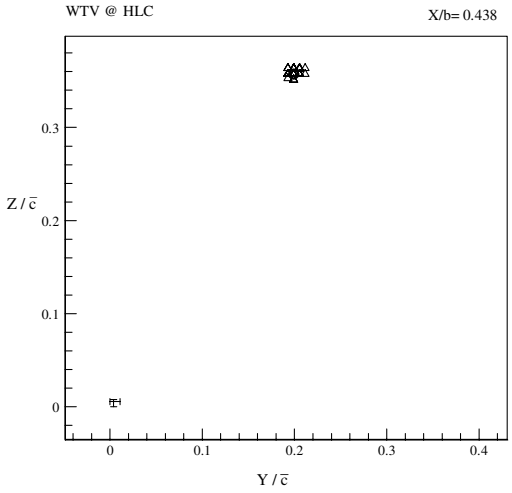

a) Scattering of wing-tip vortex center at HLC

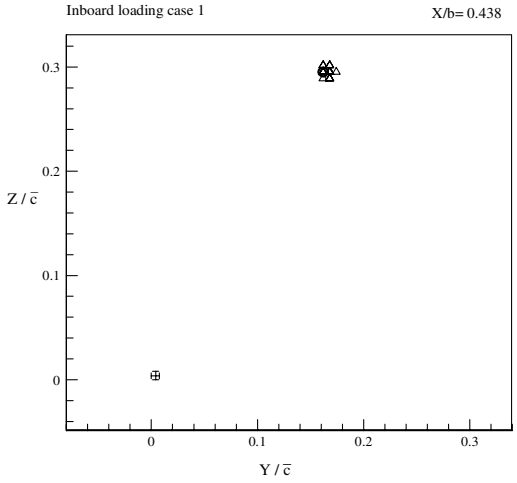

b) Wing-tip vortex center at inboard loading case 1

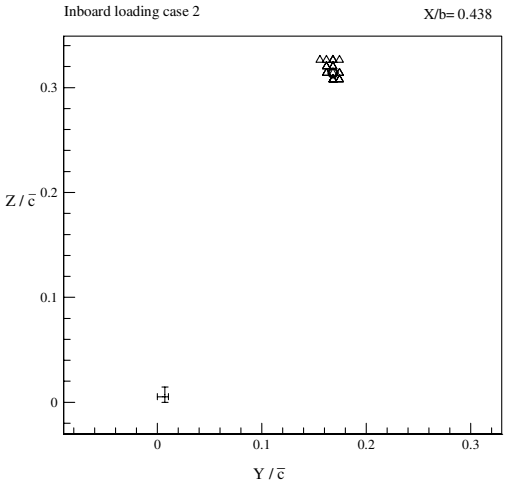

c) Wing-tip vortex center at inboard loading case 2

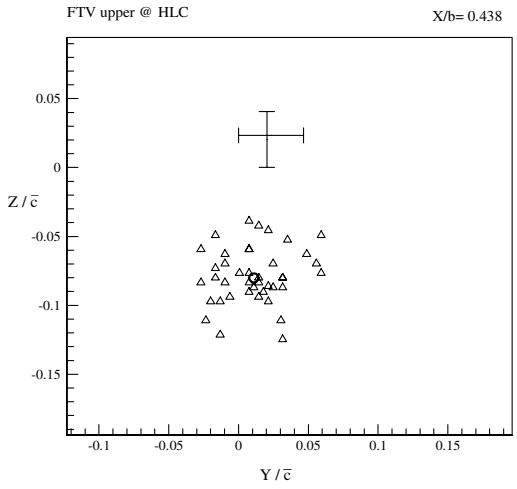

d) Scattering of flap-tip vortex center at HLC

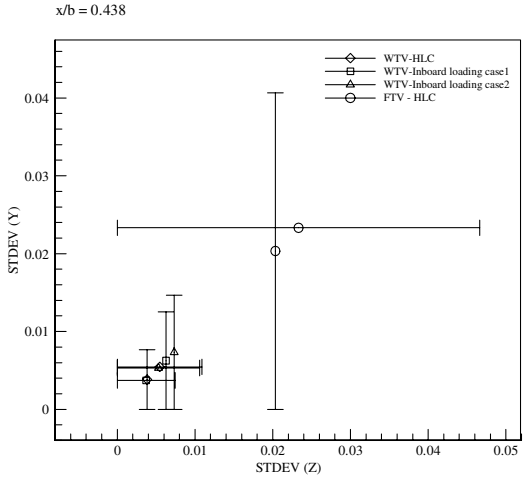

e) Standard deviation of the vortex core movement

Fig. 6 Scattering of instantaneous and averaged vortex centers a–d) and standard deviation of the vortex core movement e).

Furthermore, circulation can be defined as

$$\Gamma_{j+1/2,k+1/2} = \frac{1}{2}(v_{j,k} + v_{j+1,k})\Delta y + \frac{1}{2}(w_{j+1,k} + w_{j+1,k+1})\Delta z - \frac{1}{2}(v_{j+1,k+1} + v_{j,k+1})\Delta y - \frac{1}{2}(w_{j,k+1} + v_{j,k})\Delta z \quad (6)$$

Hence the local circulation measured at a given spanwise y, position in the wake is calculated by summing the circulation obtained at all k values (varying z) in the grid for a given j value (fixed y). This process is repeated over the whole grid giving the circulation distribution across the body in question.

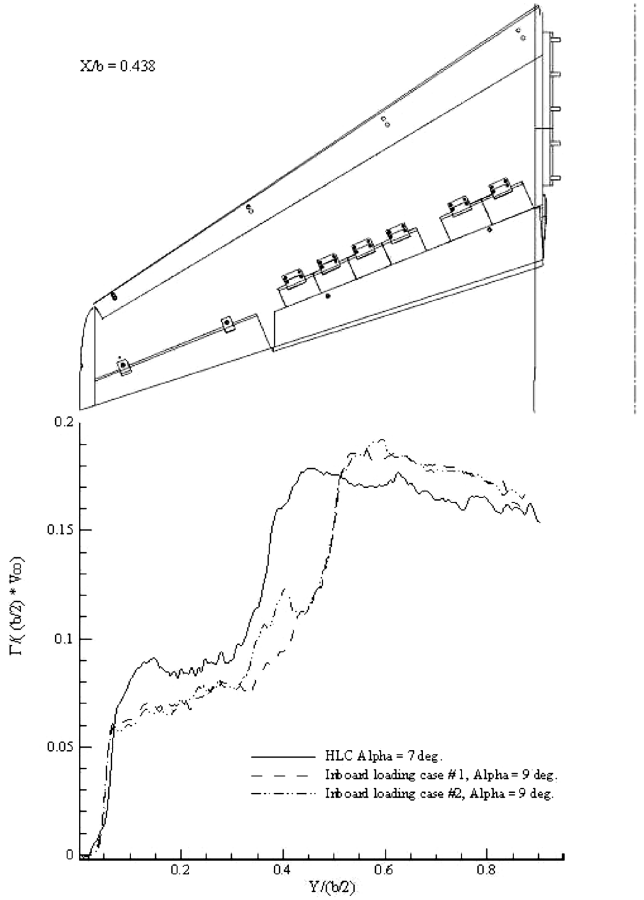

Fig. 7 Spanwise wing loads at $x/b = 0.438$, for HLC and inboard loading cases at $Re = 2.82 \times 10^5$.

A. Inboard Wing Loading

From wake surveys in a wind tunnel at $x/b = 0.438$, it is possible to derive the spanwise wing loading as reported by [12]. Figure 7 shows results of a nondimensional spanwise circulation distribution for HLC along with the two inboard wing loading cases. Wing load distribution starts from zero at the wing tip and increases due to the wing-tip and flap tip vortices reaching the maximum value at the area of the main flap wake and ends with a decrease in the circulation distribution where the fuselage is integrated to the wing. The jumps in the span load are an indication of the strength of individual vortices at this position.

The same trend of circulation distribution was followed when the spoiler numbers 5 and 6 were deflected, with a noticeable inboard shift of loading towards the fuselage for both cases. Drop of the circulation distribution and less steepness of the distribution profile slope in region of outer flap edge appears to be an evidence of the interaction of the latter with the deflected spoilers. Interaction that results in dispersion of circulation over a large area in the wake due to viscosity dominated transport mechanism, hence vortices are widened and maximum induced rolling moment encounters by a following aircraft expected to decreases at various rates. The effects of DSS in terms of circulation distribution and circulation dispersion were further enhanced for the inboard loading case 2, in which the spoiler numbers 5 and 6 were deflected at 40°. Finally the areas enclosed by circulation distribution curves remain almost unchanged for all investigated cases, since the target lift coefficient value was kept the same.

Location of the spoiler number 5 and 6 in the proximity of the main flap outer tip allows their wake to directly interact with the strong flap vortex at the early stage of vortex sheet formation. Consequently increasing diffusion of vorticity and producing flap tip vortex with larger cores is expected.

B. Effects of the DSS on Crossflow Velocity of the Flap Tip Vortex

For the evaluation of the different inboard loading cases, area at a downstream distance of $x/b = 0.438$ comprising the flap vortex is shown in Fig. 8a–8c, contour variables is the crossflow velocity $v_c = (w^2 + v^2)^{1/2}$ in 20 levels $0 \text{ m/s} < V_c < 5 \text{ m/s}$, the baseline configuration shown in Fig. 8a, yields a concentrated vortex with an approximate diameter (deduced from the maximum crossflow velocity value to the minimum crossflow velocity value and presented by a circle superimposed on the contour plot) of about $d/b = 0.59\%$ and a maximum crossflow velocity of $V_{c\text{-Max}}/V_\infty = 38.3\%$ and minimum crossflow velocity $V_{c\text{-Min}}/V_\infty = 8.3\%$.

The deflection of the spoilers leads to the enlarged vortex diameter see Fig. 8b and 8c, with about $d/b = 1.61\%$ and a maximum crossflow velocity of $V_{c\text{-Max}}/V_\infty = 21.6\%$ and minimum crossflow velocity $V_{c\text{-Min}}/V_\infty = 1.6\%$ for inboard loading case 1.

Likewise inboard loading case 2 give slightly less vortex diameter of about $d/b = 1.37\%$ and a maximum crossflow velocity of $V_{c\text{-Max}}/V_\infty = 27\%$ and minimum crossflow velocity $V_{c\text{-Min}}/V_\infty =$ 1.6%. DSS effects in terms of normalized vortex diameter, normalized maximum and minimum crossflow velocities are further summarized in Fig. 9 in term of percentage column presentation for the seek of clarity.

Those results indicates that the inboard loading case 1 results in a vortex with an increased size of about 2.73 times the size of baseline configuration while the maximum and minimum crossflow velocities were decreased by 16.7 and 6.7% compared with that of the baseline configuration, respectively. Moreover for the inboard loading case 2 an increase in the vortex size by 2.32 times the size of baseline configuration was observed while the maximum and minimum crossflow velocities were decreased by 11.3 and 6.7% compared with that of the baseline configuration, respectively. In conclusion it can be stated that DSS combines the effect of vortex size enlargement (redistribution of circulation on a wider area) with an alleviation of the crossflow velocity.

C. Effects of DSS on the Vorticity Distribution of the Flap Tip Vortex

Typical vorticity plots with their respective interpolated velocity vectors with the downstream variation of $x/b = 0.317, 0.438, 0.649$ and 1.062, are shown in Fig. 10a–10d. Vectors are presented in term of vector heads and every second vector is shown for seek of clarity. All vorticity values were nondimensionalized by multiplying values by $(b/2)/V_\infty$. Normalized peak vorticity values are marked in each respective drawing. Introduction of the DSS configurations proves to affect the structure of the flap tip vortex by combining the effect of an oscillating tip vortex (relatively high wandering amplitude of tip vortex core) with alleviation of the peak vorticity and crossflow velocity.

The ratios of normalized vorticity peak for inboard loading cases to the normalized vorticity peak of the baseline configuration at $x/b = 0.317$, 0.438, 0.649 and 1.062, are $(\xi_{\text{Peak}})_{\text{Inboard load case1}}/(\xi_{\text{Peak}})_{\text{Base-line config.}} = 80$, 58, 54.5 and 42.8% and $(\xi_{\text{Peak}})_{\text{Inboard load case2}}/(\xi_{\text{Peak}})_{\text{Base-line config.}} = 60$, 66.6 72.7 and 28.5%. This result indicates the noticeable decrease in the vorticty peak values with the downstream vortex traveling. Columns in Fig. 11 present the ratios of the vorticity peak for inboard load cases to that of the baseline configuration as a function of the downstream distance. A noticeable decrease in the vorticity peak values with the vortex traveling in the downstream direction for both inboard load cases is evidenced.

D. Effects of DSS on the Flap Tip Vortex Strength

The normalized crossflow velocity and normalized total circulation of the flap vortex changed noticeably with the spanwise wing load modification at $x/b = 0.438$ as shown in Fig. 12a and 12b.

The values of those changes are as follows: $(v_{\theta\max}/V_\infty)_{\text{Base-line config.}} = 37.9\%$ while $(v_{\theta\max}/V_\infty)_{\text{Inboard loading case1}} =$ 23.27% and $(v_{\theta\max}/V_\infty)_{\text{Inboard loading case2}} = 23\%$ and $(\Gamma_o/V_\infty\bar{c})_{\text{Base-line Config.}} = 0.357$ while $(\Gamma_o/V_\infty\bar{c})_{\text{Inboard loading case1}} =$ 0.123 and $(\Gamma_o/V_\infty\bar{c})_{\text{Inboard loading case2}} = 0.1588$. This will result in

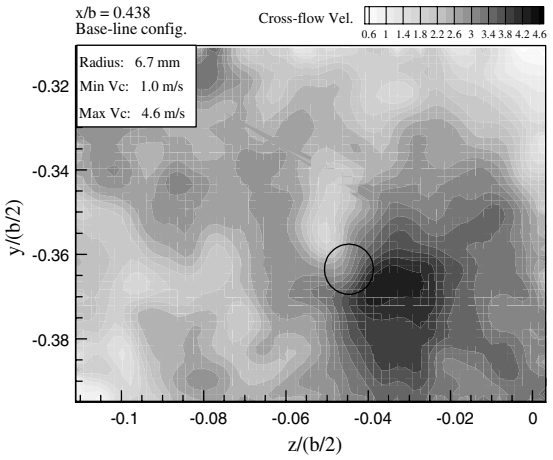

a) Cross flow velocity at HLC

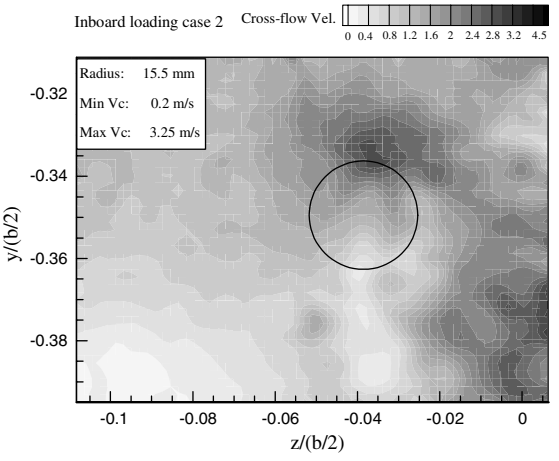

b) Cross flow velocity for inboard loading case 1

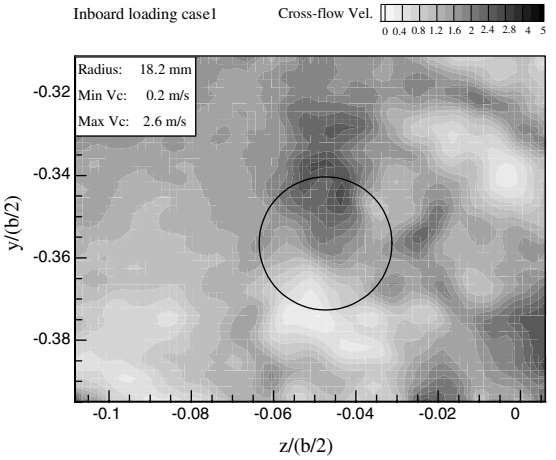

c) Cross flow velocity for inboard loading case 1

Fig. 8 Crossflow velocity distribution for flap tip vortex.

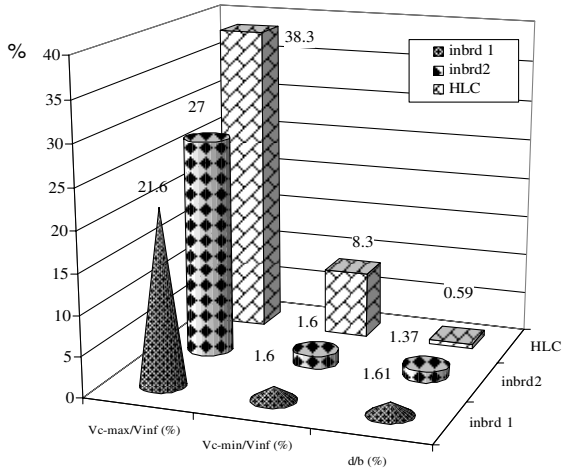

Fig. 9 Effects of inboard loading cases in term of vortex size, maximum and minimum crossflow velocities.

reduced maximum crossflow velocity and circulation for both inboard load cases by a noticeable value. This may be attributed to the interaction of the spoiler.

E. Effects of DSS on the Wing-Tip Vortex

The wing tip experiences the effect of modified wing span loading but does not show appreciable differences, both in terms of crossflow velocity and local circulation distribution, as shown in Fig. 13a and 13b. Evaluation of this effect in terms of normalized maximum crossflow velocity at $x/b = 0.438$, are $(v_{\theta\max}/V_\infty)_{\text{Base-line config.}} = 66.6\%$ for the baseline configuration while $(v_{\theta\max}/V_\infty)_{\text{Inboard loading case1}} = 59.2\%$ for inboard loading case 1 and $(v_{\theta\max}/V_\infty)_{\text{Inboard loading case2}} = 60.5\%$ for inboard loading case2. Moreover the effect on the normalized total circulation at $x/b = 0.438$ are $(\Gamma_o/V_\infty \bar{c})_{\text{Base-line Config.}} = 0.267$ for baseline configuration while $(\Gamma_o/V_\infty \bar{c})_{\text{Inboard loading case1}} = 0.2289$ for the inboard loading case 1 and finally $(\Gamma_o/V_\infty \bar{c})_{\text{Inboard loading case2}} = 0.262$ for the inboard loading case2. Those values show a slight change in the values of both normalized maximum crossflow velocity and normalized total circulation.

This fact may be explained by the distances between the flow at the deflected spoiler region and the flow at the wig tip region. Thus the level of interferences between the spoiler wake and the wing-tip vortex is rather low in the region measured until $x/b = 1.062$.

V. Wake Vortex Alleviation

To evaluate the hazard the generated wake vortex poses to a following aircraft, the induced rolling moments on a rectangular virtual following wing were computed using PIV measured velocity fields. Those velocity fields were generated by the half model strong flap edge vortex at HLC and inboard load cases. The simulated rectangular follower wing is located at (y, z), a span of $b_f/b_g = 0.2$ is chosen, subscript f refer to follower wing while subscript g stands for the generating wing. The (y', z') coordinates system is fixed with respect to the follower wing and has its origin at the wing center. The rolling moment coefficient can be expressed as

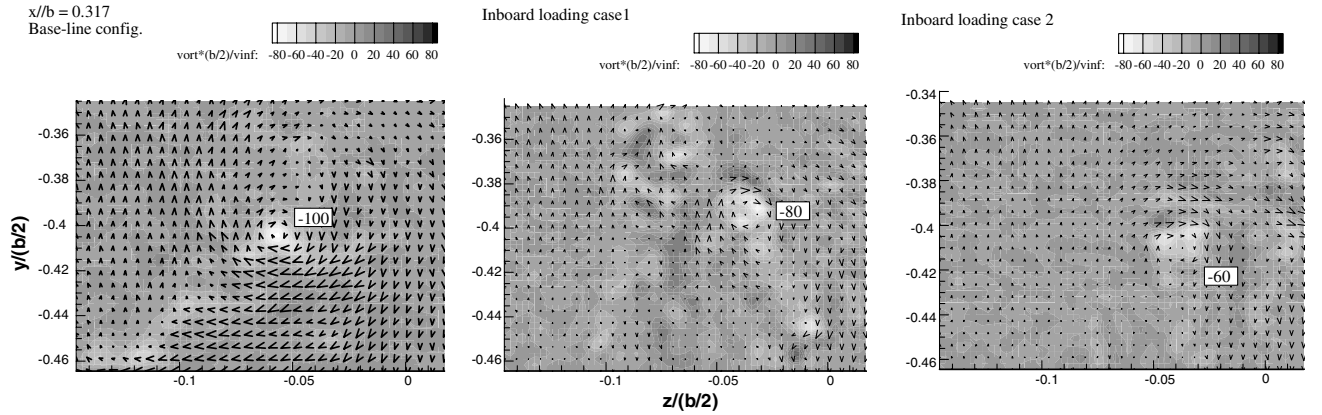

a) Inboard loading case 2 at x/b=1.062 downstream distance

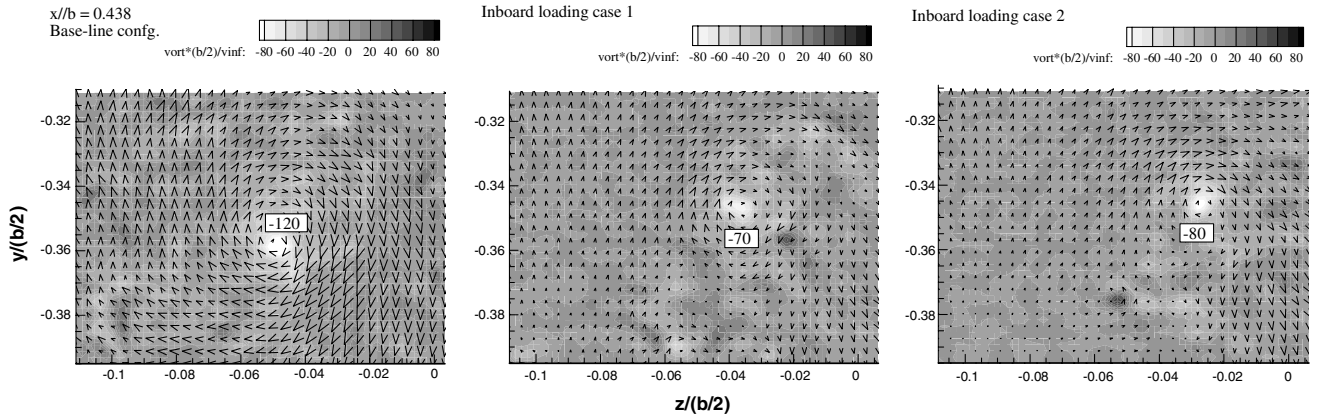

b) Inboard loading case 2 at x/b=0.438 downstream distance

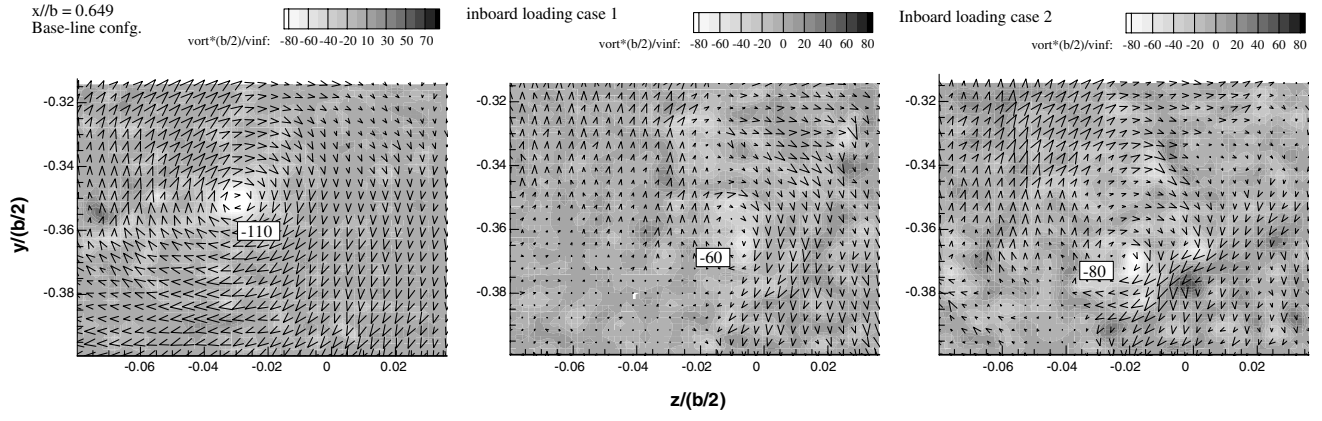

c) Inboard loading case 2 at x/b=0.649 downstream distance

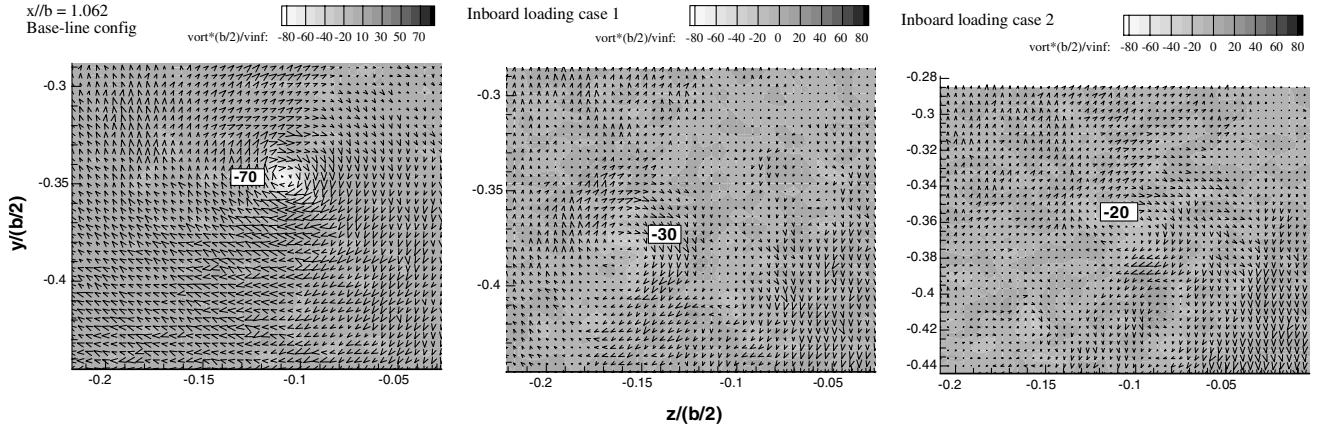

d) Inboard loading case 2 at x/b=1.062 downstream distance

Fig. 10 Instantaneous velocity vectors and normalized vorticity contours distribution of flap tip vortex.

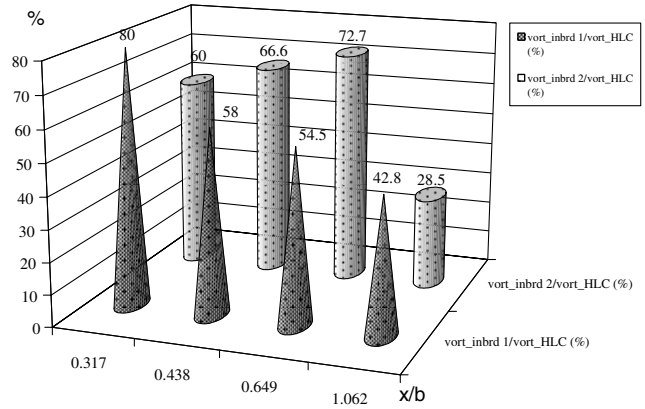

Fig. 11 Percentage of vorticity ratios for the flap tip vortex.

$$C_{lf} = C_{l\alpha f}/b_f^2 \int_{-b_f/2}^{b_f/2} y'(w/V_\infty)\,\mathrm{d}y' \tag{7}$$

where $C_{l\alpha f}$ is the two-dimensional lift curve slope usually taken as 2π for simplicity. By varying the location (y', z') of following wing, and calculating the rolling moment coefficient using Eq. (7) repeatedly over the entire flow field, yields a two-dimensional distribution of the rolling moment coefficient on the follower wing. Typical induced rolling moment coefficient distributions for HLC and inboard loading cases at the range of downstream distances $x/b = 0.317$ to 1.062 are shown in Fig's 14a–14d. As expected the maximum induced rolling moments are encountered in the region of the flap tip vortex. However, the y-z position of the maximum induced rolling moments is little influenced by the DSS it remains near the flap tip vortex. Aircraft typically have control capability to create rolling moment coefficients between (0.04–0.06) [13], so that any imposed torque by a vortex that causes C_{lf} to exceed 0.06 will cause the encountering aircraft to roll even when full counter-roll control is imposed. Computed induced rolling moment coefficients exceed the full roll control capabilities in the vortex centers for almost all investigated HLC while for the alleviated vortex with DSS those values were brought within the limit of the aircraft control capability.

A. Maximum Induced Rolling Moment

In Fig. 15, the maximum induced rolling moments $C_{lf\,\max}$ on a following rectangular wing are presented as a function of the downstream distances. For all tested configurations the maximum induced rolling moment $C_{lf\,\max}$ shows a high value at the trailing edge ($x/b = 0.317$) caused by higher levels of downwash of the

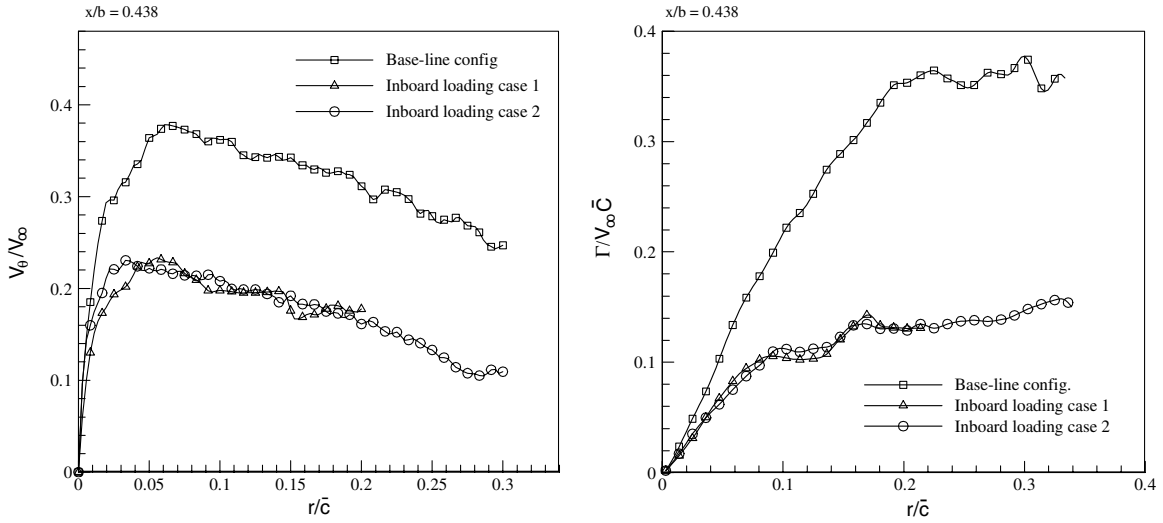

a) (v_θ/V_∞) versus ($r/\bar{c}$) **b) ($\Gamma/V_\infty c$) versus ($r/\bar{c}$)**

Fig. 12 Effects of inboard loading on flap tip vortex normalized tangential velocity and local strength.

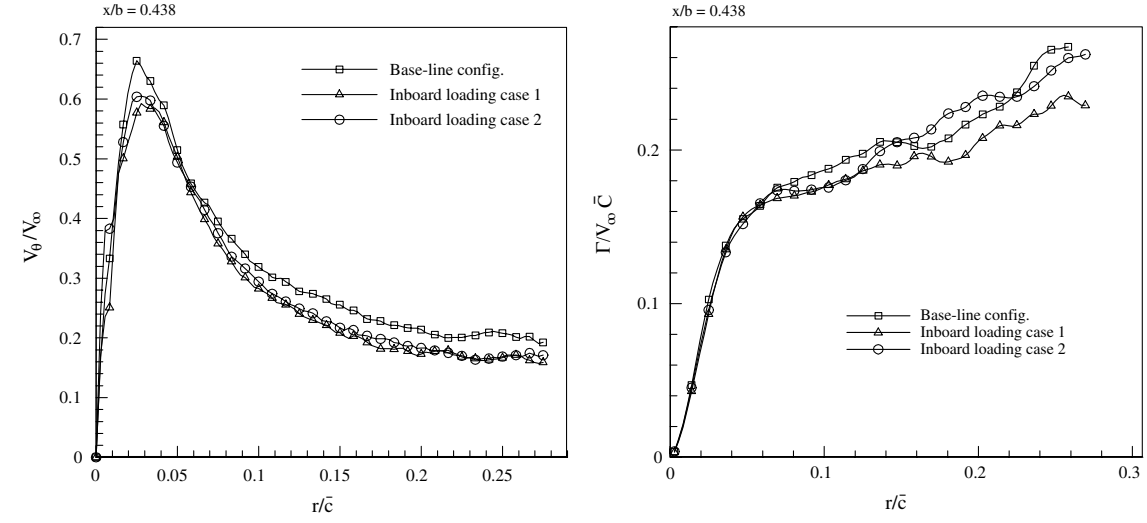

a) (v_θ/V_∞) versus ($r/\bar{c}$) **b) ($\Gamma/V_\infty c$) versus ($r/\bar{c}$)**

Fig. 13 Effects of inboard loading of wing-tip vortex normalized tangential velocity and local strength.

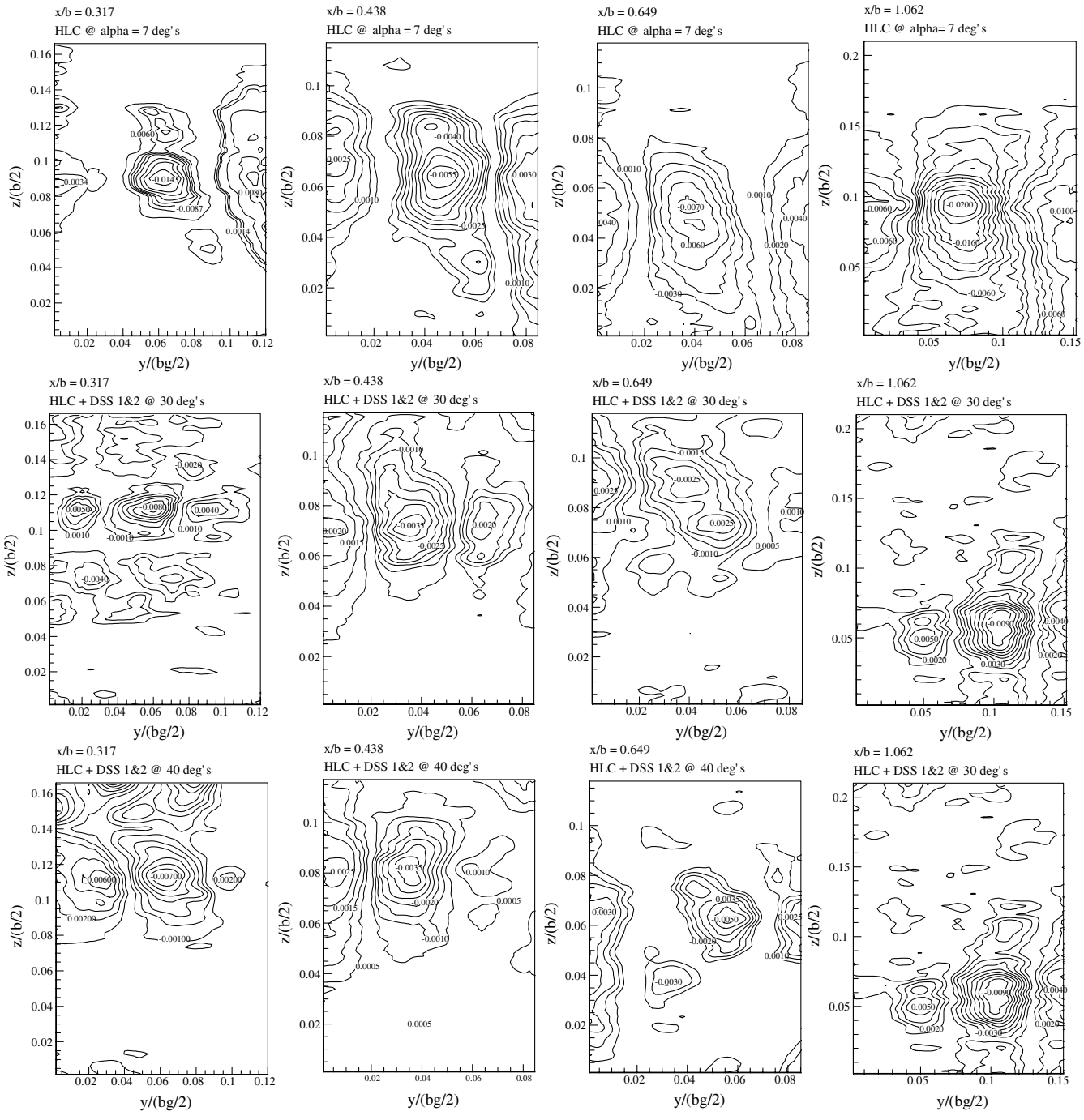

a) x/b = 0.317 **b) x/b = 0.438** **c) x/b = 0.649** **d) x/b = 1.062**

Fig. 14 Induced rolling moment coefficient (C_{lf}) on a following aircraft.

bound vortices in addition to the velocity induction of the trailing vortices.

Then, a more or less steep fall is followed by a monotonic increase in maximum induced rolling moment. The diminishing factor of the induced rolling moment is the decreasing downwash of the bound vortices further downstream of the wing. However, due to the increment of the induced velocities of the flap vortex the induced rolling moment is increases. The diffused wake structure with deflected spoilers has a strong influence on the maximum induced rolling moments $C_{lf\,\max}$ for a following aircraft ($b_f/b_g = 0.2$).

To evaluate the a mount of wake vortex alleviation, ratios of the maximum induced rolling moment coefficient of inboard load cases to that of the HLC were evaluated for the investigated range of the downstream distances. Values are as follows: $C_{lf\,\max\text{-Inb. load case1}}/C_{lf\,\max\text{-Base-line config}} = 56$, 64, 36 and 45% and $C_{lf\,\max\text{-Inb. load case2}}/C_{lf\,\max\text{-Base-line config}} = 42$, 64, 71 and 45%. Those values reveal that DSS reduces the maximum induced rolling moment $C_{lf\,\max}$ at the range of downstream distances for both inboard loading cases by a noticeable amount. This result suggests that the turbulence in the wake of the DSS has a strong influence on the induced rolling moment.

VI. Conclusions

In this work, the influence of the DSS on the wake vortex hazard reduction has been studied. DSS results in a spanwise wing loading modification (inboard loading) along with the direct interaction of the spoiler's wake and wing/ flap tips vortices. Introducing spoiler wake in the flow field increases the vortex wandering amplitude value (higher than 170% of the flap vortex radius core), which can lead to an accelerated vortex breakdown especially when the vortex motion intensifies further downstream.

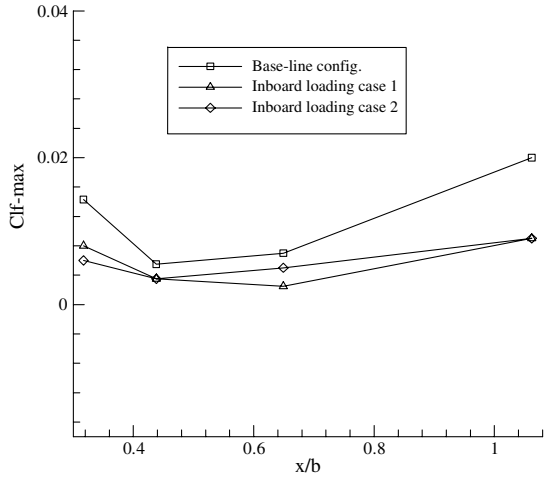

Fig. 15 $C_{lf\,\max}$ vs x/b.

The results of the inboard loading case 1 show that substantial redistribution of the flap tip vortex circulation can be achieved by the merger of the spoiler turbulent wake/flap tip vortex. A diameter of the merged vortex increased by a factor of up to 2.72 times, relative to the undisturbed flap tip vortex. Inspection of the cross-stream distribution of axial vorticity for the same case shows up to 2.33 times reduction in the peak vorticity value. A decrease of the maximum crossflow velocity by 44% relative to undisturbed flap tip vortex was also recorded for the case of deployed spoilers.

The wing-tip vortex experiences the effect of modified wing span loading but does not show appreciable differences, both in terms of crossflow velocity and local circulation distribution. This result proves that merging needs sufficient proximity between the spoiler wake turbulence and the wing/flap tip vortices or a sufficient downstream distance. Inboard loading case 2 proves to have similar effects on the flap tip vortex although inboard load case 1 showed a better response in terms of flap tip vortex diffusion along with rotational velocity and peak vorticity reduction. It can be concluded that spoiler effectiveness was obtained at a deflection angle of 30°.

Wake vortex alleviation due to DSS was evaluated in term of the induced rolling moment coefficient. Distribution of the rolling moment coefficient for inboard loading case 1 reveals that while position of the maximum induced rolling moments is little influenced by the DSS, the maximum induced rolling moment coefficient was reduced to nearly one third relative to the undisturbed flap tip vortex value.

References

[1] Crouch, J. D., "Airplane Trailing Vortices and Their Control," *Comptes Rendus-Physique*, Vol. 6, Nos. 4–5, 2005, pp. 487–499.

[2] Ciffone, D. L., "Vortex Interactions in Multiple Vortex Wakes Behind Aircraft," *Journal of Aircraft*, Vol. 14, No. 5, 1977, pp. 440–446. doi:10.2514/3.58800

[3] Corsiglia, V. R., Rossow, V. J., Ciffone, D. L., "Experimental Study of the Effect of Span Loading on Aircraft Wakes," *Journal of Aircraft*, Vol. 13, No. 12, 1976, pp. 968–973. doi:10.2514/3.58737

[4] Coustols, E., Stumpf, E., Jacquin, L., Moens, F., Vollmers, H., and Gerz, T., "Minimised Wake: A Collaborative Research Programme on Aircraft Wake Vortices," AIAA Paper 2003-0938, 41st Aerospace Sciences Meeting and Exhibit, Reno, NV, 2003.

[5] Rennich, S. C., and Lele, S. K., "Method for Accelerating the Destruction of Aircraft Wake Vortices," *Journal of Aircraft*, Vol. 36, No. 2, 1999, pp. 398–404. doi:10.2514/2.2444

[6] Ortega, J. M., Bristol, R. L., and Savas, O., "Experimental Study of the Instability of Unequal-Strength Counter-Rotating Vortex Pairs," *Journal of Fluid Mechanics*, Vol. 474, No. 12003, pp. 35–84.

[7] Bruin, A. C., and Schrauf, G., "Wake Vortex Results From the AWIATOR Project. Executive Summary," NLR Rept. No. TP-2007-527.

[8] Croom, D. R., "The Development and Use of Spoilers as Vortex Attenuators," NASA SP-409, Washington, D.C., 1976, pp. 339–368.

[9] Croom, D. R., "Low-Speed Wind-Tunnel Investigation of Various Segments of Flight Spoilers as Trailing-Vortex-Alleviation Devices on a Transport Aircraft Model," NASA TN D-8162, Washington, D.C., 1976.

[10] Bruin, A. C., and Spalart, P. R., "Flow Field Survey in Trailing Vortex System Behind a Civil Aircraft Model at High Lift: The Characterization and Modification of Wakes from Lifting Vehicles in Fluid," AGARD CP 584, 1997.

[11] Anderson, J. D., *Fundamentals of Aerodynamics*, 2nd ed., McGraw–Hill, New York, 1991.

[12] Grant, I., McCutcheon, G., McColgan, A. H., and Hurst, D., "Optical-Velocimetry, Wake Measurements of Lift and Induced Drag on a Wing," *Optics and Lasers in Engineering*, Vol. 44, Nos. 3–42006, pp. 282–303. doi:10.1016/j.optlaseng.2005.04.002

[13] Rossow, V. J., "Inviscid Modelling of Aircraft Trailing Vortices," NASA SP-409, *NASA Symposium on Wake Vortex Minimization*, Washington, D.C., 1976, pp. 4–54.